UNIVERSITY OF AMSTERDAM

UvA-DARE (Digital Academic Repository)

Axion-photon conversion in neutron star magnetospheres

The role of the plasma in the Goldreich-Julian model

Witte, S.J.; Noordhuis, D.; Edwards, T.D.P.; Weniger, C.

DOI
10.1103/PhysRevD.104.103030

Publication date
2021

Document Version
Other version

Published in
Physical Review D

License
CC BY

Link to publication

Citation for published version (APA):
Witte, S. J., Noordhuis, D., Edwards, T. D. P., & Weniger, C. (2021). Axion-photon conversion in neutron star magnetospheres: The role of the plasma in the Goldreich-Julian model. *Physical Review D*, *104*(10), [103030]. https://doi.org/10.1103/PhysRevD.104.103030

General rights
It is not permitted to download or to forward/distribute the text or part of it without the consent of the author(s) and/or copyright holder(s), other than for strictly personal, individual use, unless the work is under an open content license (like Creative Commons).

Disclaimer/Complaints regulations
If you believe that digital publication of certain material infringes any of your rights or (privacy) interests, please let the Library know, stating your reasons. In case of a legitimate complaint, the Library will make the material inaccessible and/or remove it from the website. Please Ask the Library: https://uba.uva.nl/en/contact, or a letter to: Library of the University of Amsterdam, Secretariat, Singel 425, 1012 WP Amsterdam, The Netherlands. You will be contacted as soon as possible.

UvA-DARE is a service provided by the library of the University of Amsterdam (https://dare.uva.nl)

Download date:27 Jul 2022

Axion-Photon Conversion in Neutron Star Magnetospheres:

Supplemental Material

Appendix A: Photon Dispersion Equation

In this section we outline the derivation of the generalized dispersion relation relevant for the propagation of radio waves near the surface of neutron stars. First, we derive the dispersion relation for a cold and non-relativistic plasma (for a detailed overview, see *e.g.* [64] and references therein), and then generalize the derivation to the case where electrons and positrons have non-negligible boosts in the plasma rest frame.

We begin by writing down the linear equations of motion for non-relativistic charged particles in the presence of an external electromagnetic field, given by

$$m_s \frac{d\vec{v}_s}{dt} = q_s(\vec{E} + \vec{v}_s \times \vec{B})\,, \tag{A1}$$

where we have introduced the subscript s to denote the species (*e.g.* electron, positron, proton, etc). The relevant Maxwell equations can be expressed as[17]

$$\nabla \times \vec{E} = -\frac{\partial \vec{B}}{\partial t}\,, \tag{A2}$$

$$\nabla \times \vec{B} = \left(4\pi \vec{J} + \frac{\partial \vec{E}}{\partial t}\right)\,. \tag{A3}$$

Here the current is given by $\vec{J} \equiv \sum_s q_s\, n_s\, \vec{v}_s$ and n_s is the number density. We can now assume an isotropic and homogeneous plasma, and take a plane wave ansatz for the fields as $\vec{E} = \vec{E}_1\, e^{i(\vec{k}\cdot\vec{r}-\omega t)}$, $\vec{B} = \vec{B}_0 + \vec{B}_1\, e^{i(\vec{k}\cdot\vec{r}-\omega t)}$, and $\vec{v} = \vec{v}_1\, e^{i(\vec{k}\cdot\vec{r}-\omega t)}$, where $\vec{B}_0$ is the static background magnetic field. We furthermore take $\vec{B}_0$ to be in the $\hat{z}$ direction and assume that the magnitude $B_0 \gg B_1$. Using Eqs. (A1-A3), one can solve for the various components of the current density

$$J_\pm = i\epsilon_0 \sum_s \frac{\omega_{p,s}^2}{m_s\,(\omega \mp \Omega_s)}\, E_\pm\,, \tag{A4}$$

$$J_z = i\epsilon_0 \sum_s \frac{\omega_{p,s}^2}{\omega}\, E_z\,. \tag{A5}$$

Here, we have introduced the $E_\pm$ notation to define $E_\pm \equiv E_x \pm iE_y$ (and similarly for the velocity and current vectors). We have also defined the cyclotron frequency of species s as $\Omega_s \equiv q_s B_0/m_s$; for the plasma of interest here, the dominant species are electrons and positrons, and thus $\Omega_s = \mp\Omega_e$.

The dielectric tensor $\boldsymbol{\epsilon}$ is generically defined as

$$\boldsymbol{\epsilon} = \mathbb{I} - 4\pi \frac{\boldsymbol{\sigma}}{i\omega}\,, \tag{A6}$$

where the conductivity $\boldsymbol{\sigma}$ can be inferred from the current equation $\vec{J} = \boldsymbol{\sigma}\cdot\vec{E}$. With the current as defined in Eq. (A4), one can express the dielectric tensor as

$$\begin{aligned}
\epsilon_{xx} = \epsilon_{yy} &= 1 - \sum_s \frac{\omega_{p,s}^2}{\omega^2 - \Omega_s^2}\,,\\
\epsilon_{xy} = -\epsilon_{yx} &= \sum_s \frac{\Omega_s\, \omega_{p,s}^2}{\omega(\omega^2 - \Omega_s^2)}\,,\\
\epsilon_{zz} &= 1 - \sum_s \frac{\omega_{p,s}^2}{\omega^2}\,,\\
\epsilon_{xz} = \epsilon_{zx} = \epsilon_{yz} = \epsilon_{zy} &= 0\,.
\end{aligned} \tag{A7}$$

[17] In this section we will work with Gaussian units and take $c = 1$ (the latter being adopted throughout the text).

Maxwell's equations given in Eq. (A2) can be expressed in terms of the dielectric tensor as

$$i\vec{k} \times \vec{E} = i\omega \vec{B}\,, \tag{A8}$$

$$i\vec{k} \times \vec{B} = i\omega \boldsymbol{\epsilon} \cdot \vec{E}\,. \tag{A9}$$

Combining these equations yields the so-called wave equation, given by

$$\vec{n} \times (\vec{n} \times \vec{E}) + \boldsymbol{\epsilon} \cdot \vec{E} = 0\,, \tag{A10}$$

where $\vec{n} = \vec{k}/\omega$ is the index of refraction. Without loss of generality, we can take $\vec{k}$ to lie in the x-z plane; in this case, the dispersion relations of propagating electromagnetic modes can be directly determined by solving

$$\begin{vmatrix} n^2\cos^2\theta - \epsilon_{xx} & -\epsilon_{xy} & -n^2\cos\theta\sin\theta - \epsilon_{xz} \\ -\epsilon_{yx} & n^2 - \epsilon_{yy} & -\epsilon_{yz} \\ -n^2\cos\theta\sin\theta - \epsilon_{zx} & -\epsilon_{zy} & n^2\sin^2\theta - \epsilon_{zz} \end{vmatrix} = 0\,, \tag{A11}$$

where we have defined θ as the angle between $\vec{k}$ and $\vec{B}_0$. In the low frequency and large magnetic field limit, which equates to $|\Omega_e| \gg \omega, \omega_p$, one finds the following three dispersion relations

$$\omega^2 = k^2\,, \tag{A12}$$

$$\omega^2 = \frac{1}{2}\left(k^2 + \omega_p^2 - \sqrt{k^4 + \omega_p^4 - 2k^2\omega_p^2(1 - 2\cos^2\theta)}\right)\,, \tag{A13}$$

$$\omega^2 = \frac{1}{2}\left(k^2 + \omega_p^2 + \sqrt{k^4 + \omega_p^4 - 2k^2\omega_p^2(1 - 2\cos^2\theta)}\right)\,. \tag{A14}$$

These correspond to the magnetosonic-t, Alfvén, and Langmuir-O mode, respectively (see *e.g.* [65]).

The dispersion relations above are derived assuming a non-relativistic plasma. In order to determine whether our calculations are robust against this assumption, we now derive generalized dispersion relations for charged species with arbitrary phase space distributions. This discussion largely follows the work of [65, 91–93] and the references therein. As before, we will work in the low frequency and strong magnetic field limit. In addition to taking $|\Omega_e| \gg \omega, \omega_p$, the assumption of a strong magnetic field allows one to focus on plasma distribution functions that are one-dimensional (oriented along the magnetic field lines).

We begin by generalizing the equations of motion for charged particles in an external electromagnetic field. In full generality, the evolution of the distribution function of a species f_s is given by the Vlasov equation [65, 92, 93]

$$\frac{\partial f_s}{\partial t} + \vec{v}\frac{\partial f_s}{\partial \vec{r}} + \frac{q_s}{m_s}(\vec{E} + \vec{v} \times \vec{B})\frac{\partial f_s}{d\vec{u}} = 0\,, \tag{A15}$$

where $\vec{u} = \vec{v}\gamma$ is the proper velocity and $\gamma = 1/\sqrt{1 - v^2}$. Note that we still take $\vec{B} = \vec{B}_0 + \vec{B}_1$, with the background field $\vec{B}_0$ being oriented along the z-axis and much larger than $\vec{B}_1$. The charge density and current density can be defined in terms of the distribution functions using

$$\rho = \sum_s q_s \int d^3u\, f_s(\vec{u})\,, \tag{A16}$$

$$\vec{J} = \sum_s q_s \int d^3u\, \vec{v}\, f_s(\vec{u})\,. \tag{A17}$$

In order to solve Maxwell's equations, it is useful to expand the phase space distribution in cylindrical velocity coordinates as

$$f_s = \sum_{n=-\infty}^{\infty} f_{s,n}(u_\perp, u_z) e^{-inu_\phi}\,. \tag{A18}$$

By rewriting the Vlasov equation, this expansion allows one to write a single equation governing the evolution of each mode $f_{s,n}$

$$(L_n + in\tilde{\Omega}) f_n + \sum_{\sigma=\pm1} G_\sigma^{n-\sigma} f_{n-\sigma} = 0\,, \tag{A19}$$

where the subscript s has been omitted for clarity. The operators L_n and G^n_σ are given by

$$L_n = \frac{\partial}{\partial t} + v_z \frac{\partial}{\partial z} + \alpha E_z \frac{\partial}{\partial u_z} + in\alpha\gamma^{-1} B_z \,, \tag{A20}$$

$$G^n_\sigma = \frac{v_\perp}{2}\nabla_\sigma + \frac{\alpha}{2}(E_\sigma d_{\sigma n} + i\sigma B_\sigma r_{\sigma n}) \,. \tag{A21}$$

In the above we have introduced the definitions $\alpha = q/m$, $\tilde{\Omega} = \Omega_s/\gamma$, $E_\sigma = E_x + i\sigma E_y$ (the same relation holds for B and ∇), and we have defined

$$d_{\sigma n} = \frac{\partial}{\partial u_\perp} - \frac{\sigma n}{u_\perp} \,,$$
$$r_{\sigma n} = v_z d_{\sigma n} - v_\perp \frac{\partial}{\partial u_z} \,.$$

One can also write the charge and current densities in terms of the moments f_n, which yield

$$\rho = \sum_s q_s \int du_\perp du_z \, u_\perp f_{s,0} \,, \tag{A22}$$

$$J_z = \sum_s q_s \int du_\perp du_z \, u_\perp v_z f_{s,0} \,, \tag{A23}$$

$$J_\sigma = J_x + i\sigma J_y = \sum_s q_s \int du_\perp du_z \, u_\perp v_\perp f_{s,\sigma} \,. \tag{A24}$$

In this notation, Maxwell's equations can be expressed as

$$\frac{i}{2}\sum \sigma \nabla_\sigma E_{-\sigma} = -\frac{\partial}{\partial t} B_z \,, \tag{A25}$$

$$\frac{\partial}{\partial z} E_\sigma - \nabla_\sigma E_z = \frac{\partial}{\partial t}(i\sigma B_\sigma) \,, \tag{A26}$$

$$\frac{-1}{2}\sum \nabla_\sigma (-i\sigma B_{-\sigma}) = \frac{\partial}{\partial t} E_z + 4\pi J_z \,, \tag{A27}$$

$$\frac{\partial}{\partial z}(i\sigma B_\sigma) - i\sigma \nabla_\sigma B_z = \frac{\partial}{\partial t} E_\sigma + 4\pi J_\sigma \,, \tag{A28}$$

$$\frac{1}{2}\sum \nabla_\sigma E_{-\sigma} + \frac{\partial}{\partial z} E_z = 4\pi\rho \,, \tag{A29}$$

$$\frac{i}{2}\sum \sigma \nabla_\sigma (-i\sigma B_{-\sigma}) + \frac{\partial}{\partial z} B_z = 0 \,. \tag{A30}$$

Up until now the analysis is still completely general and while the above equations are no easier to solve than the original versions, our notation has clarified that the current density is fully defined by knowing only f_0 and f_σ. In order to identify these terms, we can exploit the low frequency approximation in which a small parameter $\xi \sim \omega\gamma/|\Omega_s| \ll 1$ is introduced through the substitution $\Omega_s \to \Omega_s/\xi$. With this substitution, Eq. (A19) can be written as

$$\begin{aligned} L_0 f_0 &= -\sum_\sigma G^\sigma_{-\sigma} f_\sigma \,, \\ f_n &= \frac{\xi}{in\tilde{\Omega}}\left[- L_n f_n - \sum_\sigma G^{n-\sigma}_\sigma f_{n-\sigma} \right] \text{for } |n| \geqslant 1 \,. \end{aligned} \tag{A31}$$

Due to the equilibrium distribution being gyrotropic [65], all f_n with $|n| \geqslant 1$ should vanish if $\vec{E} \to 0$, $\vec{B} \to 0$ and $\nabla \to 0$. Looking at the second of the above equations, this fact tells us that these f_n cannot contain terms dependent on negative powers of ξ. Furthermore, the overall form of Eq. (A31) shows that all terms in a given f_n have to be at least one order of ξ higher than the lowest order term in f_{n-1}. As a result, it is possible to represent the phase space distribution in the following way

$$f_n = \sum_{m=|n|}^{\infty} \xi^m \, f_n^{(m)} \,. \tag{A32}$$

One thus needs to start by determining f_0, and all higher order f_n can subsequently be found through Eq. (A31). We can further expand in the weak turbulence limit, $\eta \sim E/B_0 \ll 1$ [65], and keep only terms up to orders ξ^2 and η, which is enough for our purposes. This allows us to write f_0 and f_σ in the general forms

$$f_0 = F_0(u_\perp, u_z) + \eta \sum_{n=0}^{2} \xi^n f_0^{(n)} \,, \tag{A33}$$

$$f_\sigma = \eta \sum_{n=1}^{2} \xi^n f_\sigma^{(n)} \,. \tag{A34}$$

Additionally, working up to order ξ^2, and plugging Eq. (A32) into Eq. (A31) results in

$$\begin{aligned} L_0 f_0 &= \sum_\sigma G^\sigma_{-\sigma} \frac{\xi}{i\sigma\tilde{\Omega}} \left(1 - \frac{\xi L_\sigma}{i\sigma\tilde{\Omega}}\right) G^0_\sigma f_0 \,, \\ f_\sigma &= \frac{-\xi}{i\sigma\tilde{\Omega}} G^0_\sigma f_0 + \left(\frac{\xi}{i\sigma\tilde{\Omega}}\right)^2 L_\sigma G^0_\sigma f_0 \,. \end{aligned} \tag{A35}$$

If we now switch to Fourier space and assume space-time dependencies given by $\exp(i\vec{k}\cdot\vec{r} - i\omega t)$, the above equations can be combined to derive explicit expressions for both f_0 and f_σ. They are given by

$$f_0 = F_0(u_\perp, u_z) - \frac{\alpha k_\perp v_\perp}{2\tilde{\Omega}\zeta} E_y \mu_0 F_0 + \frac{i\alpha k_\perp v_\perp}{2\tilde{\Omega}^2 \omega} E_x \mu_0 F_0 + \frac{i\alpha k_\perp^2 v_\perp v_z}{2\tilde{\Omega}^2 \zeta} E_z \mu_0 F_0 + \frac{i\alpha k_\perp v_\perp}{2\tilde{\Omega}^2} E_x \mu_0 F_0 \,, \tag{A36}$$

$$f_\sigma = \frac{i\alpha}{2\sigma\tilde{\Omega}} [E_\sigma + E_z(k_\perp v_z/\zeta)] \mu_0 F_0 + \frac{\alpha k_\perp^2 v_\perp^2}{4\sigma\tilde{\Omega}^2\zeta} E_y \mu_0 F_0 + \frac{i\alpha\zeta}{2\tilde{\Omega}^2} [E_\sigma + E_z(k_\perp v_z/\zeta)] \mu_0 F_0 \,. \tag{A37}$$

Here we used that $\vec{B} = \vec{k} \times \vec{E}/\omega$ and introduced the parameters $\zeta = \omega - k_z v_z$ and $\mu_0 = [\zeta(\partial/\partial u_\perp) + k_z v_\perp (\partial/\partial u_z)]/\omega$. Notice that the artificial parameter ξ previously introduced to justify the expansion of Eq. (A31) has also been set to 1, justifying the validity of the above procedure.

At this point, one can directly compute the current density, and subsequently the dielectric tensor. Pulling out the density normalization from $F_{s,0}$, such that $\int d^3u F_{s,0} = 1$, the generalized dielectric tensor is given by

$$\begin{aligned} \epsilon_{xx} &= 1 - \sum_s \frac{\omega_{p,s}^2}{2\omega\Omega_s^2} \int du_\perp du_z \, u_\perp^2 \gamma\zeta\mu_0 F_{s,0} \,, \\ \epsilon_{yy} &= \epsilon_{xx} + \sum_s \frac{\omega_{p,s}^2 k_\perp^2}{4\omega\Omega_s^2} \int du_\perp du_z \, u_\perp^4 \gamma^{-1}\zeta^{-1}\mu_0 F_{s,0} \,, \\ \epsilon_{zz} &= 1 + \sum_s \frac{\omega_{p,s}^2}{\omega} \int du_\perp du_z \, u_\perp v_z \zeta^{-1} \frac{\partial F_{s,0}}{\partial u_z} - \sum_s \frac{\omega_{p,s}^2 k_\perp^2}{2\omega\Omega_s^2} \int du_\perp du_z \, u_\perp^2 u_z^2 \gamma^{-1}\zeta^{-1}\mu_0 F_{s,0} \,, \\ \epsilon_{xy} &= -\epsilon_{yx} = i \sum_s \frac{\omega_{p,s}^2}{2\omega\Omega_s} \int du_\perp du_z \, u_\perp^2 \mu_0 F_{s,0} \,, \\ \epsilon_{xz} &= \epsilon_{zx} = -\sum_s \frac{\omega_{p,s}^2 k_\perp}{2\omega\Omega_s^2} \int du_\perp du_z \, u_\perp^2 u_z \mu_0 F_{s,0} \,, \\ \epsilon_{yz} &= -\epsilon_{zy} = i \sum_s \frac{\omega_{p,s}^2 k_\perp}{2\omega\Omega_s} \int du_\perp du_z \, u_\perp^2 u_z \zeta^{-1} \mu_0 F_{s,0} \,, \end{aligned} \tag{A38}$$

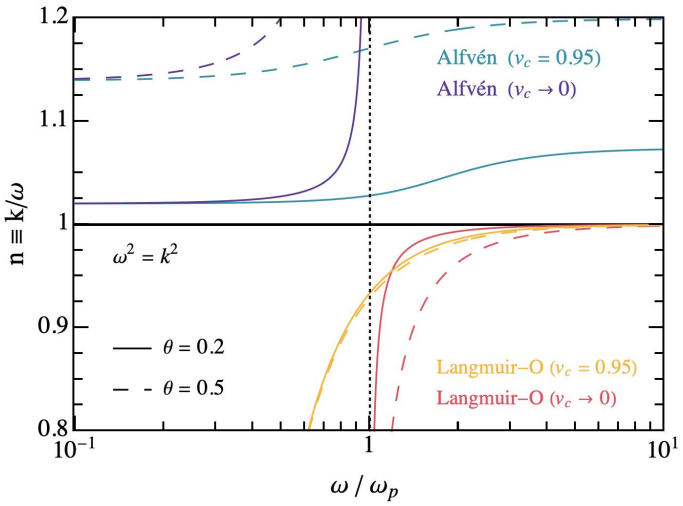

FIG. 5. Comparison of the three electromagnetic modes present in the infinite magnetic field limit (note that the magnetosonic-t mode in this limit is synonymous with the free space mode, $\omega^2 = k^2$). The Alfvén and Langmuir-O modes are shown for waves propagating at an angle $\theta = 0.2$ (solid) and 0.5 (dashed) radians with respect to the magnetic field. Both modes are shown taking the limit of a non-relativistic plasma (red, purple) and for a Waterbag distribution with cut-off velocity $v_c = 0.95$ (see Eq. (A42)). The vertical dotted line identifies the branch cut in the non-relativistic Langmuir-O mode arising at $\omega = \omega_p$.

Focusing on leading order terms in the low frequency limit, Eq. (A38) reduces to

$$\begin{aligned}
\epsilon_{xx} &= \epsilon_{yy} = 1 + \mathcal{O}\left(\frac{\omega_{p,s}^2}{\Omega_s^2}\right) , \\
\epsilon_{zz} &= 1 + \sum_s \frac{\omega_{p,s}^2}{\omega} \int du_\perp du_z \, u_\perp v_z \zeta^{-1} \frac{\partial F_{s,0}}{\partial u_z} + \mathcal{O}\left(\frac{\omega_{p,s}^2}{\Omega_s^2}\right) , \\
\epsilon_{xy} &= -\epsilon_{yx} = \mathcal{O}\left(\frac{\omega_{p,s}^2}{\omega\Omega_s}\right) , \\
\epsilon_{xz} &= \epsilon_{zx} = \mathcal{O}\left(\frac{\omega_{p,s}^2}{\Omega_s^2}\right) , \\
\epsilon_{yz} &= -\epsilon_{zy} = \mathcal{O}\left(\frac{\omega_{p,s}^2}{\omega\Omega_s}\right) .
\end{aligned} \tag{A39}$$

Some of these corrections contain thermal terms that can partially remove the suppression. Near the neutron star surface where the thermal corrections may be large, however, one expects the cyclotron frequency to be $\Omega_e \sim 4 \times 10^6$ eV, which is about 10 orders of magnitude larger then the maximum frequency we are interested in. It therefore seems safe to neglect the higher order terms in Eq. (A39), even in the presence of large thermal corrections. This means that in the end we will only need to evaluate one term, namely

$$I \equiv \sum_s \frac{\omega_{p,s}^2}{\omega} \int du_\perp du_z \, u_\perp v_z \zeta^{-1} \frac{\partial F_{s,0}}{\partial u_z} \, . \tag{A40}$$

To this end, we start by taking the thermal plasma distribution to be one-dimensional, *i.e.* $F_{s,0}(u_\perp, u_z) = \tilde{F}_{s,0}(u_z)\delta(u_\perp)/u_\perp$ with normalization $\int du_z \tilde{F}_{s,0} = 1$. Computing this remaining function yields

$$I(\omega, \theta, n) = \sum_s \frac{\omega_{p,s}^2}{\omega^2} \int du_z \, \frac{1}{n_\parallel} \frac{1}{1 - n_\parallel v_z} \frac{d\tilde{F}_{s,0}}{du_z} \, , \tag{A41}$$

where we have defined $n_\parallel = k_z/\omega = n\cos\theta$. To further simplify this expression one must define the shape of the one-dimensional distribution function. Since we are interested in studying the general behavior or the dispersion

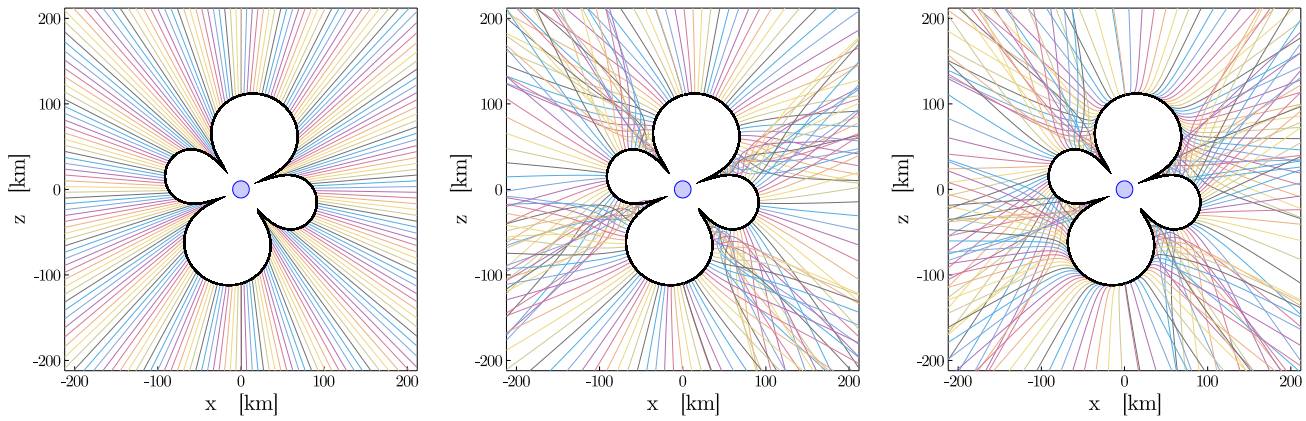

FIG. 6. Result of ray-tracing photon trajectories from source location at the conversion surface (black contour) of a neutron star, assuming a GJ model of the magnetosphere. Photons are sourced in the $x-z$ plane (with $\vec{k} = 10^{-3} m_a \hat{r}$), allowed to propagate in three dimensions, and projected back into the $x-z$ plane. The three panels correspond to dispersion relations $\omega^2 = k^2$, $\omega^2 = k^2 + \omega_p^2$, and Eq. (1).

relation, we adopt an intuitively straightforward distribution for both electrons and positrons called the Waterbag distribution [94]. This assumes a linear flat distribution in velocities up to a cut-off u_c, *i.e.*

$$\tilde{F}_{s,0} = \frac{1}{2u_{c,s}} \Theta(u_{c,s}^2 - u_z^2)\,. \tag{A42}$$

With this assumption, the integral in Eq. (A41) becomes

$$I(\omega, \theta, n) = -\sum_s \frac{\omega_{p,s}^2}{\omega^2} \frac{1}{\gamma_{c,s}(1 - n_{||}^2\, v_{c,s}^2)}\,, \tag{A43}$$

with γ_c and v_c being the cut-off gamma factor and velocity respectively. We can now directly solve for the dispersion relations using Eq. (A11). In this case, the magnetosonic-t modes remain unaltered by boosts, but the roots associated with the Alfvén and Langmuir-O are now obtained by solving the following

$$\omega^2 = \frac{(n_{||}^2 - 1)\,\cos^2\theta}{n_{||}^2 - \cos^2\theta} \sum_s \frac{\omega_{p,s}^2}{\gamma_{c,s}(1 - n_{||}^2\, v_{c,s}^2)}\,. \tag{A44}$$

One can nicely see that in the limit $v_c \to 0$ and $\gamma_c \to 1$, the non-relativistic dispersion relations for the Alfvén and Langmuir-O modes are recovered. An alternative limit of interest is that of a single relativistic species. In this case, the dispersion relation of the Langmuir-O mode is given by

$$\omega^2 = \frac{1}{2\gamma_c^2}\left(k^2(\gamma_c^2 + \cos^2\theta(\gamma_c^2 - 1)) + \gamma_c \omega_p^2 + \sqrt{k^4(\gamma_c^2 - \cos^2\theta(\gamma_c^2 - 1))^2 - 2k^2\omega_p^2\gamma_c(\cos^2\theta + \gamma_c^2(\cos^2\theta - 1)) + \gamma_c^2\omega_p^4}\right)\,. \tag{A45}$$

Notice that in the limit where $\cos\theta \ll 1$, photons follow the non-relativistic dispersion relation with the replacement $\omega_p \to \omega_p/\sqrt{\gamma_c}$. In addition, in the limit $\gamma \to \infty$, one recovers the free space distribution $\omega^2 = k^2$. This leads to the important observation that the inclusion of a boosted plasma is likely to reduce the importance of the various effects studied in this work.

We demonstrate the behavior of the various modes that appear in the strong magnetized limit in Fig. 5. Here, we plot the spectral index as a function of the frequency (in units of ω_p) for each of the modes at angles of $\theta = 0.2$ and 0.5 radians with respect to the magnetic field. For both the Alfvén and Langmuir-O modes, we show the impact of taking a Waterbag distribution with cut-off velocity $v_c = 0.95$; the primary effect is to lower (raise) the branch cut of the Langmuir-O (Alfvén) mode, such that a larger range of frequencies can propagate. The vertical dotted line highlights the branch cut that appears in the Langmuir-O mode at $\omega = \omega_p$. Photons sourced from axion conversion on the Langmuir-O mode trajectories will tend to travel to the right in the phase diagram as they escape the magnetosphere, and will quickly tend toward to the free space dispersion relation. Importantly, Fig. 5 illustrates that modes do not cross, and thus remain well-defined and isolated in the strong field limit.

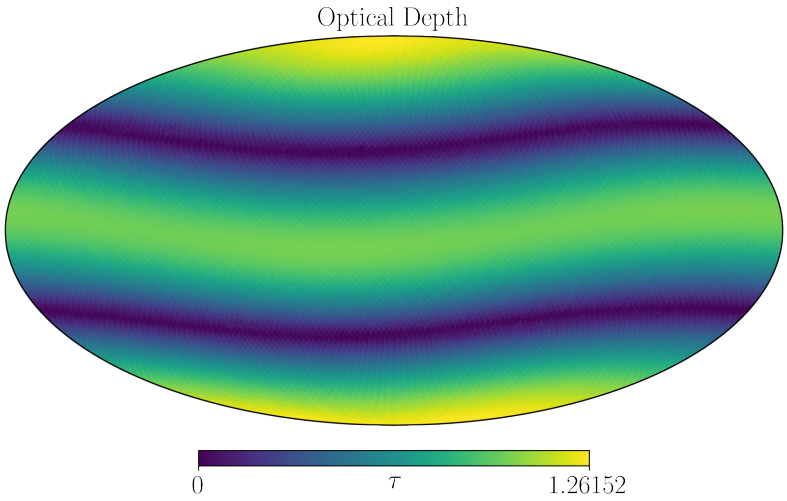

FIG. 7. Optical depth τ for neutron star with $B_s = 5 \times 10^{14}$ G, $\omega_{NS} = 1\,\mathrm{s}^{-1}$, $\theta_m = 0.2$, and for an axion mass $m_a = 10^{-6}$ eV. Since the rate is suppressed by $e^{-\tau}$, one can see that for these parameters the optical depth is beginning to suppress the flux coming from the lobes and torus, but leaves the flux coming from the throats effectively untouched.

In order to illustrate the importance of adopting the correct dispersion relation – and in tracking the individual photon trajectories – we show in Fig. 6 the evolution of photons in the x-z plane propagating away from a neutron star conversion surface using either the free space dispersion relation $\omega^2 = k^2$ (left), cold plasma dispersion relation $\omega^2 = k^2 + \omega_p^2$ (center), or the non-relativistic highly-magnetized plasma dispersion relation given in Eq. (1) (right). All photons are sourced with $\vec{k} = 10^{-3} m_a \, \hat{r}$, where $\hat{r}$ is the unit vector directed from the origin toward the point of genesis. One can see that the angular inhomogeneities in the plasma frequency of the GJ model generate enormous anisotropic features in the photon trajectories. The impact of accounting for the magnetized nature of the plasma is more subtle, however; this effect is most apparent near the magnetic poles, where photon trajectories can experience strong refraction.

Appendix B: Cyclotron Resonance

The dominant absorption process of low energy radio photons escaping the magnetosphere occurs via the cyclotron resonance, in which electrons in the ambient plasma are excited to higher Landau orbitals. For strong magnetic fields and relativistic plasmas, this occurs when [69–71]

$$\omega - k_{||} v_{||} - \Omega_e / \gamma = 0 \,, \tag{B1}$$

where $k_{||} = k \cos\tilde{\theta}$, $v_{||}$ is the velocity of the plasma in the direction of the magnetic field, and Ω_e is the electron cyclotron frequency. Since the magnetic field falls off as $B \propto r^{-3}$, one expects all photons to cross the cyclotron resonance – for non-relativistic plasmas this occurs at a fixed distance, while for relativistic distributions this may take place over an extended region. We show here that, in the simplified context of the GJ model, the cyclotron resonance is not necessarily negligible. We begin by noting that for non-relativistic plasmas the second term in Eq. (B1) can be neglected, and γ can be set to one. The optical depth of photons scattering of ambient electrons and positrons is given by

$$\tau = \int d\ell \, \sigma \, n_e \,, \tag{B2}$$

where the cross section (assuming $\omega \ll m_e$) for non-relativistic cyclotron absorption is given by [69]

$$\sigma = (2\pi)^2 \, r_e \, \delta \left(\omega - \Omega_e \right) \,. \tag{B3}$$

Here, $r_e \equiv \alpha / m_e$ is the classical electron radius. Assuming the photon frequency is approximately constant, we find

$$\tau = \pi \left(\frac{\omega_p^2}{\omega} \right) \left. \frac{\omega}{|\partial_\ell \Omega_e|} \right|_{\ell = \ell_c} \,. \tag{B4}$$

If one assumes outward radial trajectories this can be approximated as

$$\tau \sim \frac{\pi}{3}\left(\frac{\omega_p^2}{\omega}\right)\ell_c\,. \tag{B5}$$

Here, ℓ_c is the location of the resonance along the path. Importantly, in the above we have assumed that the resonance condition is met within the light cone with radius $R_{LC} = 1/\omega_{NS}$, otherwise we set the optical depth to zero. We illustrate the optical depth τ as a function of sky position in Fig. 7 for a strong magnetic field model with $B_s = 5\times 10^{14}\,\mathrm{G}$. In this case, photons originating from either the bulge or the torus have an optical depth $\tau \sim 1$, and thus experience a suppression of the flux on the level of $\sim 60\%$. This effect can be far more extreme for larger magnetic fields and larger rotational speeds.

Appendix C: Revisiting the Conversion Probability

An important result of this paper is the correction of the conversion probability adopted in previous works (see main text). There are two problems which have gone overlooked: (*i*) the angular contribution to the conversion length, and (*ii*) the de-phasing of the photon and axion wave functions which results from non-linear photon propagation. In order to be clear on the origin of each effect, we review the derivation of the conversion probability before highlighting where the novel effects enter. The equations detailing the propagation of electromagnetic waves in the presence of axions, at leading order in the axion-photon coupling constant $g_{a\gamma\gamma}$, are given by

$$\begin{aligned} -\nabla^2\vec{E} + \nabla(\nabla\cdot\vec{E}) &= -\partial_t^2(\boldsymbol{\epsilon}\cdot\vec{E}) - g_{a\gamma\gamma}\vec{B}_0\partial_t^2 a\,, \\ (\partial_t^2 - \nabla^2 + m_a^2)a &= g_{a\gamma\gamma}\vec{E}\cdot\vec{B}_0\,, \end{aligned} \tag{C1}$$

where m_a is the axion mass, $\boldsymbol{\epsilon}$ is the dielectric tensor, and $\vec{B}_0$ is the local magnetic field. These expressions are derived from Maxwell's equations coupled to axions, assuming a constant background magnetic field $\vec{B}_0$. If we furthermore work in the high magnetization and low frequency limit, *i.e.* $|\Omega_e| \gg \omega, \omega_p$, the dielectric tensor takes the form (see Appendix A for derivation)

$$\boldsymbol{\epsilon} = R_\theta^{xz}\cdot\begin{pmatrix}1 & 0 & 0\\ 0 & 1 & 0\\ 0 & 0 & \epsilon_{zz}\end{pmatrix}\cdot R_{-\theta}^{xz}\,, \tag{C2}$$

where $\epsilon_{zz} = 1-\omega_p^2/\omega^2$ and the rotation matrix is given by

$$R_\theta^{xz} = \begin{pmatrix}\cos\theta & 0 & \sin\theta\\ 0 & 1 & 0\\ -\sin\theta & 0 & \cos\theta\end{pmatrix}\,. \tag{C3}$$

Without loss of generality we have taken the external magnetic field to lie in the first quadrant of the x-z plane, at an angle θ from the z-axis. Moreover, we choose the photon and axion to travel along the z-axis. Notice that this is a different orientation relative to Appendix A, where previously we had chosen the magnetic field to be oriented along the z-axis and taken the photon momentum to be in the x-z plane. Nevertheless, the choice is irrelevant as our results only depend on θ. After computing the dielectric tensor in Eq. (C2), it becomes clear that the photon polarization perpendicular to the external field (E_y) fully decouples. Furthermore, we find that the solution for E_z can be re-expressed in terms of E_x. Assuming an oscillatory time dependence with frequency ω, one then obtains the following equation for the mixing between the axion and the E_x component of the electric field

$$-\partial_z^2\begin{pmatrix}E_x\\ a\end{pmatrix} = \begin{pmatrix}\frac{\omega^2-\omega_p^2}{1-\frac{\omega_p^2}{\omega^2}\cos^2\theta} & \frac{\omega^2 g_{a\gamma\gamma}B_0\sin\theta}{1-\frac{\omega_p^2}{\omega^2}\cos^2\theta}\\ \frac{g_{a\gamma\gamma}B_0\sin\theta}{1-\frac{\omega_p^2}{\omega^2}\cos^2\theta} & \omega^2-m_a^2\end{pmatrix}\cdot\begin{pmatrix}E_x\\ a\end{pmatrix}\,. \tag{C4}$$

Importantly, the general solution thus contains both a transverse and a longitudinal component, as expected for a Langmuir-O mode propagating at an oblique angle with respect to $\vec{B}_0$. The longitudinal component will naturally be damped (evolving into a fully transverse O mode) as the wave propagates away from the neutron star.

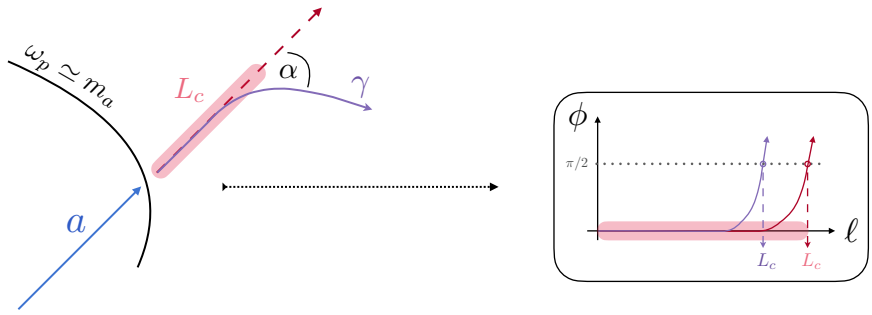

FIG. 8. Illustration of de-phasing introduced from non-linear axion trajectories. In the context of the one-dimensional formalism, the conversion length is computed from the de-phasing induced along straight-line trajectories. Should the axion trajectory deviate from this trajectory by an angle α, additional de-phasing will be introduced and the conversion length will be shortened.

After changing variables to the vector potential $A_x = -E_x/i\omega$, it is possible to adopt a plane wave ansatz and express both fields as

$$a(z,t) = a_0\, e^{i\xi(z)-i\omega t}, \qquad A_x(z,t) = \frac{A_{x,0}}{\sqrt{k_\gamma(z)}}\, e^{i\chi(z)-i\omega t}\,. \tag{C5}$$

Notice here that the photon momentum can be inferred from the dispersion relation derived in Appendix A, and in the non-relativistic limit it is given by

$$k_\gamma(z) = \sqrt{\frac{\omega^2-\omega_p^2(z)}{1-\frac{\omega_p^2(z)}{\omega^2}\cos^2\theta(z)}}\,. \tag{C6}$$

The seemingly arbitrary factor $k_\gamma^{-1/2}$ present in the photon amplitude emerges from the WKB approximation (see *e.g.* [64]). In the spirit of [95], we now expand the functions $\xi(z)$ and $\chi(z)$ in powers of the magnetic field as

$$\begin{aligned}\xi(z) &= \sqrt{\omega^2-m_a^2}\,z + \xi^{(1)}(z) + \dots\,,\\ \chi(z) &= \int_0^z dz'\; k_\gamma(z') + \chi^{(1)}(z) + \dots\,,\end{aligned} \tag{C7}$$

where we have accounted for the possibility of a strong positional dependence in the photon momentum. Employing both this expansion and the WKB approximation allows us to solve Eq. (C4) for $\chi^{(1)}$, yielding

$$\chi^{(1)}(z) = \frac{i\omega a_0}{2A_{x,0}}\int_0^z dz'\,\frac{\beta(z')}{\sqrt{k_\gamma(z')}}\; e^{i\int_0^{z'} dz''\left(\sqrt{\omega^2-m_a^2}-k_\gamma(z'')\right)}\,, \tag{C8}$$

where

$$\beta(z) \equiv \frac{g_{a\gamma\gamma}B_0(z)\sin\theta(z)}{1-\frac{\omega_p^2(z)}{\omega^2}\cos^2\theta(z)}\,. \tag{C9}$$

With this expression, one can write the photon field at a distance z (given a negligible initial field value) as

$$A_x(z,t) = -\frac{\omega a_0}{2\sqrt{k_\gamma(z)}}\; e^{i\int_0^z dz' k_\gamma(z')-i\omega t}\int_0^z dz'\,\frac{\beta(z')}{\sqrt{k_\gamma(z')}}\; e^{i\int_0^{z'} dz''\left(\sqrt{\omega^2-m_a^2}-k_\gamma(z'')\right)}\,. \tag{C10}$$

Since the energy flux of a plane wave scalar field scales like $f \propto k_a^2|a|^2$, with k_a the momentum of the axion field, the

conversion probability can be directly obtained from [42, 96][18]

$$P_{a\to\gamma} = \frac{k_\gamma(z)^2}{k_a^2}\frac{|A_x(z,t)|^2 + |A_z(z,t)|^2}{|a(0,t)|^2} = \frac{1}{\sin^2\theta}\left|\frac{A_x(z,t)}{a(0,t)}\right|^2 . \tag{C11}$$

Notice that because conversion only takes place when $k_\gamma(z) \simeq k_a$, the pre-factors approximately cancel. Equation (C10) can be integrated using the stationary phase approximation, where the phase in the integral

$$\phi \equiv \int_0^z dz' \left(k_a - k_\gamma(z')\right) \tag{C12}$$

is expanded about $\partial\phi/\partial z = 0$. Keeping the leading order term in this Taylor expansion and performing both integrals in Eq. (C10), one arrives at

$$P_{a\to\gamma} = \frac{\pi}{2v_c^2}\left(\frac{g_{a\gamma\gamma}\,B}{\sin\theta}\right)^2 |\partial_z k_\gamma|^{-1}\frac{1}{\sin^2\theta}\,, \tag{C13}$$

where v_c is the axion velocity at the conversion point. Importantly, we periodically find that conversion lengths of individual axions can be quite large – notice that this is actually quite problematic since our formalism is not valid in this regime. In order to avoid spurious features, we thus cut out photons whose conversion lengths exceed 1 km. This threshold is somewhat arbitrary, but any reasonable change in this threshold introduces effectively no change in the physical observables.

Now, as mentioned in the main text, the second derivative of the phase (and thus also the conversion probability) derived in [39, 41, 42] has been truncated at leading order in velocity. The derivative of θ, however, only appears at next-to-leading order. If the axion speed at the conversion surface were always small this would not be a problem, but for conversions near the radius of the neutron star the speed can be as large as $v_c \sim 0.5$. Consequently, the next-to-leading order correction can be rather significant, particularly for particles with non-radial orbits. Working up to second order in the velocity expansion, one finds

$$\frac{\partial k_\gamma}{\partial z} \simeq \frac{1}{v_c}\left[\left(\frac{1}{\sin^2\theta} - \frac{v_c^2}{\tan^2\theta}\right)\frac{\partial\omega_p}{\partial z} + \frac{m_a v_c^2}{\tan\theta}\frac{\partial\theta}{\partial z}\right]. \tag{C14}$$

This is related to the conversion length L_c via

$$L_c = \sqrt{\pi}\left|\frac{\partial k_\gamma}{\partial z}\right|^{-1/2} . \tag{C15}$$

Notice that if one keeps only the leading order in v_c, considers perpendicular propagation (*i.e.* $\sin\theta = 1$), and adopts the radial trajectory approximation of $\partial\omega_p/\partial z$, this result reproduces the conversion probabilities derived in Refs. [40–42]. Here, we improve upon these approximations by directly calculating both directional derivatives using auto-differentiation for each trajectory of interest, and find that deviations from the radial trajectory approximation can be significant.

The second concern that we must address is related to the fact that the three-dimensional mixing equations have not been solved (see *e.g.* [96] for recent progress in this direction). The derivation of the conversion probability had assumed a plane wave solution proportional to e^{ikz}, which amounts to a one-dimensional simplification of the more general plane wave form $e^{i\vec{k}\cdot\vec{r}}$. If photons deviate strongly from this one-dimensional projection over distances $r \lesssim L_c$, the axion and photon will no longer oscillate in phase, and the conversion probability will be markedly reduced. In order to address the importance of this effect we begin by identifying the relationship between the conversion length and the phase difference of the axion and photon in the limit where photons propagate along straight trajectories perpendicular to the external field. In this case, the phase overlap of the axion and photon is given by Eq. (C12), but now with $k_\gamma = \sqrt{\omega^2 - \omega_p^2}$. If one directly computes this phase from photon trajectories generated with the

[18] While this manuscript was in review, Ref. [96] appeared, revisiting the derivation of the conversion probability in three dimensions. This work has identified two significant corrections: (i) the factor of $1/\sin^2\theta$ appearing in Eq. (C11), arising from the longitudinal component of the vector potential, and (ii) the role of off-diagonal derivatives in Eq. (C1). We include the former factor, but defer the inclusion of the second modification to future work as this would also require revisiting the de-phasing calculation.

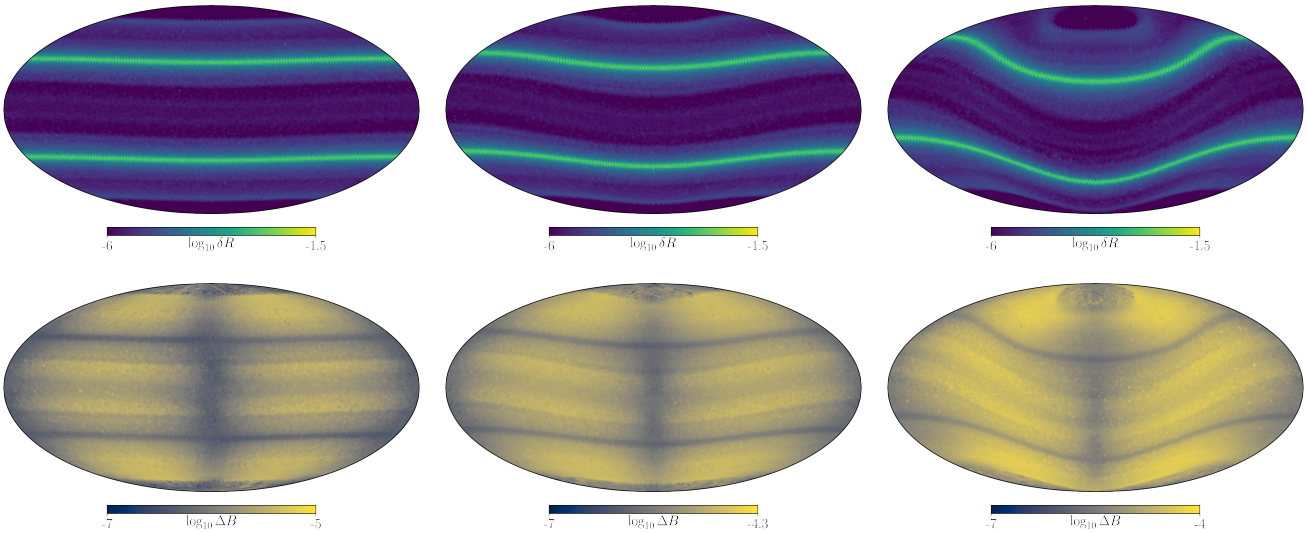

FIG. 9. Fractional rate (top) and line width (bottom) in each pixel at distances $r \sim R_{LC}$. Figures from left to right illustrate $\theta_m = 0.05$, 0.2, and 0.6 radians (note that scales are not equivalent).

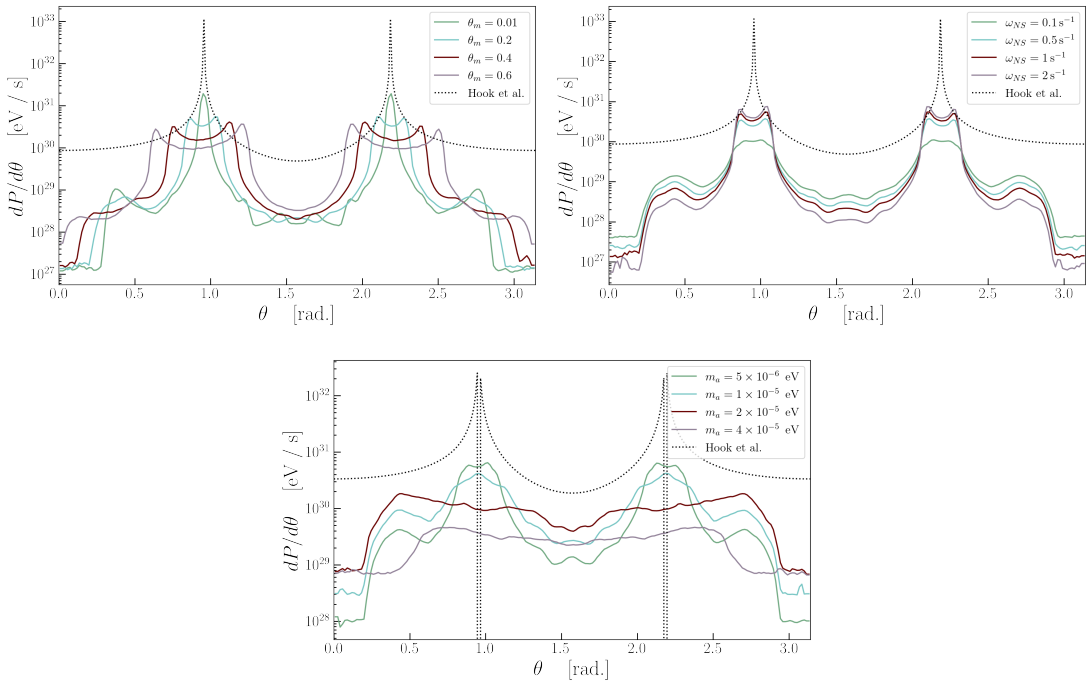

FIG. 10. Comparison of time-averaged power radiated per unit viewing angle, $dP/d\theta$, varying θ_m (top-left), ω_{NS} (top-right), and m_a (bottom). Results are shown in comparison with predictions from [39][a] (in the case of varying m_a, we fix m_a to 5×10^{-6} eV), but taking $\theta_m = 0$ (black dashed). The axion-photon coupling is taken to be $g_{a\gamma\gamma} = 10^{-12}\,\mathrm{GeV}^{-1}$, and the magnetospheres are either fixed to the fiducial values used in the main text (the case for varying θ_m and ω_{NS}) or the magnetar model (varying m_a).

[a] Importantly, as pointed out in [42], Ref. [39] is missing a factor of v_c in the radiated power. We re-introduce this factor when illustrating 'Hook et al.' results.

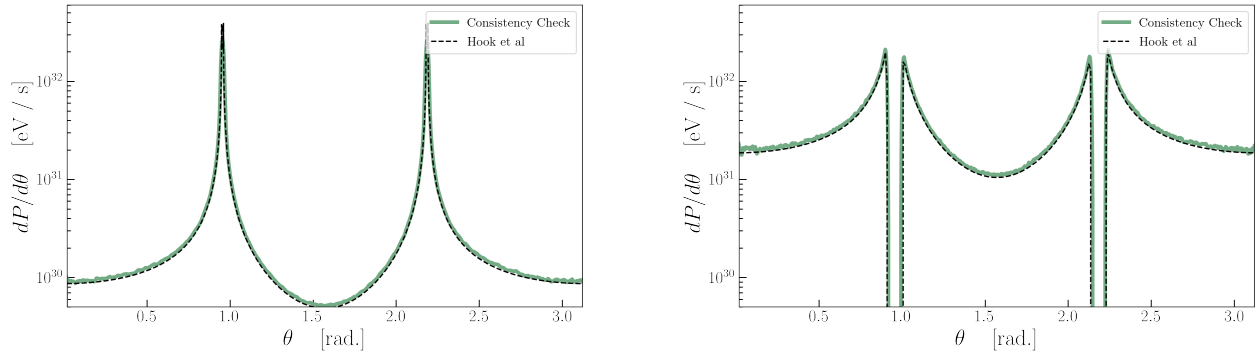

FIG. 11. Comparison of the time-integrated differential power as approximated in [39] (black), with a run in which (*i*) absorption and premature de-phasing is neglected, (*ii*) the radial derivative approximation $\partial_\ell k_\gamma \to 3m_a/(2r_c v_c)$ is applied universally, (*iii*) photons are assumed to travel radially outward, (*iv*) the size of the surface element at each point is re-scaled to be consistent with the radial approximation, and (*v*) the factor of $|\hat{v}\cdot\hat{n}|$ has been removed. The above assumptions should be roughly consistent with the approximation of [39]. Results are shown for the fiducial model used throughout this text (left) and the magnetar PSR J1745-2900 (right), but taking $\theta_m = 0.01$ and $m_a = 10^{-6}$ eV (left) and 10^{-5} eV (right), and $g_{a\gamma\gamma} = 10^{-12}\,\text{GeV}^{-1}$.

non-magnetized plasma dispersion relation (*i.e.* $\omega^2 = k^2 + \omega_p^2$), one finds that the axion-photon phase difference ϕ for all photons (which have not undergone refraction) at the conversion surface is $\phi(L_c) \sim \pi/2$. As can be seen from the derivation above, the generalization to non-perpendicular directions of the phase involves the replacement of k_γ by that given in Eq. (C6). Nevertheless, this equation still assumes that photons travel on straight line trajectories (notice that this is apparent in the ansatz in Eq. (C5)) – additional de-phasing may enter as photons refract. In order to account for this effect we approximate the de-phasing by defining a new phase overlap

$$\phi^* \equiv \int_0^\ell d\ell' \left(k_a - \cos\alpha\, k_\gamma(l')\right), \tag{C16}$$

where α is the angle between the initial axion momentum and the photon momentum after some time (and thus depends on time implicitly), and we have replaced the one-dimensional distance z by the path length ℓ. In our analysis we attempt to account for this additional de-phasing by identifying the distance each photon has traveled when $\phi^* = \pi/2$; we associate this path length with the 'corrected' conversion length L_c'. Since the conversion probability is $\propto L_c^2$, we re-weight the MC weight by a factor of $(L_c'/L_c)^2$. This procedure is illustrated schematically in Fig. 8. While a rigorous treatment of the three-dimensional mixing is required in order to robustly assess the impact of this effect, we believe that our prescription offers a reasonable estimate of its magnitude.

Appendix D: Parameter Dependence of Sky Maps

The results presented in the main text are shown for a fiducial set of parameters of the GJ model which are expected to be representative of neutron stars in the Milky Way. The purpose of this section is to address the sensitivity of the results presented to the choices of these parameters. In particular, we focus on the parameters likely to induce the largest effects; these include: the misalignment angle θ_m, the rotational frequency of the neutron star ω_{NS}, and the magnetic field strength at the surface B_s. We also discuss implications of changing the axion mass.

We begin in Fig. 9 by considering the impact of the misalignment angle on the isotropy (top) and line dispersion (bottom). Specifically we consider three choices of θ_m corresponding to 0.05 (left), 0.2 (center), and 0.6 (right) radians. The trend in the both cases is immediately apparent – larger values of θ_m induce stronger anisotropies, in particular with respect to photons produced in the throat, and larger line widths. Furthermore, large values of θ_m imply less sensitivity to the viewing angle, since the throats more broadly sweep through large areas of the sky.

Since we have discussed the impact of varying the above parameters on line width in the main text, we focus next instead on their impact on the radiated power. We illustrate in Fig. 10 the time-averaged differential power per viewing angle $dP/d\theta$, as a function of viewing angle for various parameter choices. We plot for comparison the predicted power using the formalism of Ref. [39] assuming $\theta_m = 0$ (all other parameters are either set to the fiducial values used in the main text or to those of the magnetar). We highlight two important results of these figures. Firstly,

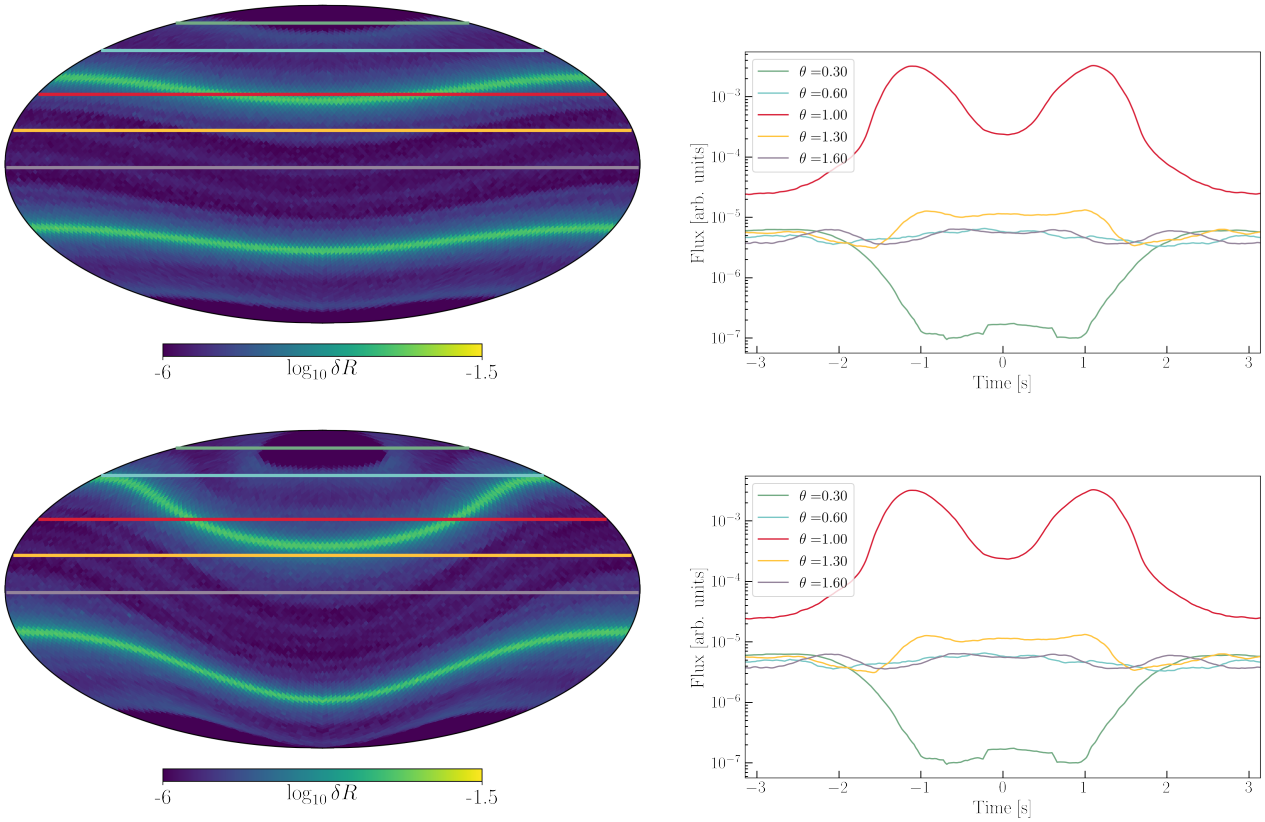

FIG. 12. Time dependence of the flux for our fiducial model (top) and model with $\theta_m = 0.6$ (bottom). The five horizontal lines shown in each sky map (left) correspond to $\theta = 0.3, 0.6, 1, 1.3, 1.6$ radians, and are translated into time-dependent fluxes (right). Results are obtained by binning over photons with $\theta = \theta_i \pm 0.02$ radians.

the flux is strongly reduced relative to previous predictions. Secondly, the sensitivity to the viewing angle is strongly increased (spanning, in some cases, nearly 5 orders of magnitude).

In order to ensure the code developed for this work is reliable, we also present a consistency check in which we attempt to reproduce the results of Ref. [39] by systematically removing the effects included here. We do this by (i) removing all absorption, (ii) removing the de-phasing cut on L_c, (iii) taking the radial derivative approximation $\partial_\ell k_\gamma \to 3m_a/(2r_c v_c)$, (iv) assuming photons sourced at some location $\vec{r}_i$ travel radially outward thereafter, (v) rescaling the size of the surface element at each point by a factor of $|\hat{n}\cdot\hat{r}|$ (this comes from the fact that [39] has a self contradictory assumption of radial trajectories that are perpendicular to the normal), and (vi) removing the factor of $|\hat{v}\cdot\hat{n}|$. As shown in Fig. 11, this procedure perfectly reproduces the results of Ref. [39]. The panels display results for the fiducial model with $\theta_m = 0.01$ and $m_a = 10^{-6}$ eV (left) and $m_a = 10^{-5}$ eV (right) (and taking $g_{a\gamma\gamma} = 10^{-12}\,\text{GeV}^{-1}$).

Appendix E: Time Dependence of Sky Maps

An important feature of the signal discussed in this work is the expected time-dependence of the flux – strong time variations allow for the signal to be more easily disentangled from spurious line signals. As mentioned in the main text, the expected time-dependence of the signal can be read off the flux maps by drawing horizontal lines and tracing the flux over a period of rotation. A single example of this procedure is illustrated in Fig. 2. In this section we present two additional illustrations to highlight the time dependence of the flux for a variety of viewing angles and two misalignment angles.

In each case we bin the flux at each value of ϕ over a narrow range of viewing angles (defined by angles of constant θ) in order to extract the flux as a function of time. Specifically, we take viewing angles of $\theta = 0.3, 0.6, 1, 1.3$, and 1.6 radians (these regions are highlighted in the left panel of Fig. 12), and a width in θ of 0.02 radians. We show the projected flux (in arbitrary units) for each slice in the right panels of Fig. 12. Depending on the viewing angle, the

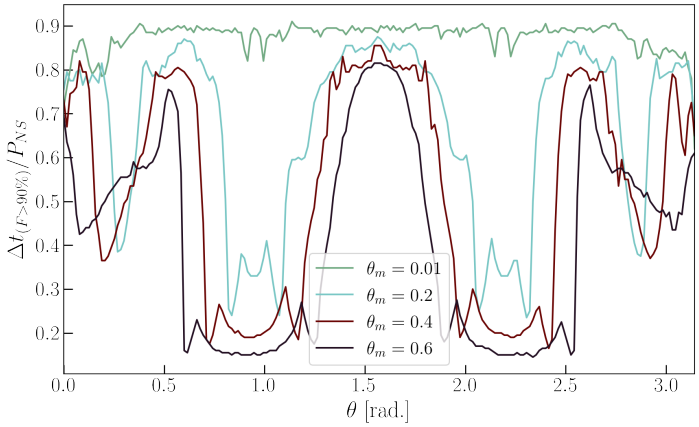

FIG. 13. Fractional time per rotational period in which 90% of the flux is generated, as a function of viewing angle θ. The four different lines correspond to four choices of θ_m.

time variation over a period can span up to a few orders of magnitude, although the likelihood of encountering such strong time variations depends crucially on the misalignment angle.

One way to quantify the strength of the time dependence is to look at the fractional part of the period over which $X\%$ of the flux is generated, with X being an arbitrarily chosen threshold which we set here to be 90. If the quantity is small, it implies that nearly the entirety of the period-averaged flux is generated in a very narrow time window, and thus the time variance must be large. Alternatively, if this fraction is close to 1, the signal must be nearly time-independent. We plot this quantity in Fig. 13 for various misalignment angles as a function of viewing angle. One can see that this fraction typically spans between 20% and 80%, and is systematically shifted toward smaller values at larger misalignment angles.

Appendix F: Convergence Checks

In this section we illustrate the approximate level of convergence achieved in our sky maps by generating many realizations under a fixed number of photon trajectories, and comparing the ratio of the standard deviation to mean $\xi_i \equiv \sigma_i/\mu_i$ in each pixel i across the different realizations. Importantly, convergent sky maps are far more complicated to generate than e.g. a converged estimate of the time-averaged differential power (per unit viewing angle), simply because the latter exploits the azimuthal symmetry. In addition, convergence is also impeded by the size of the conversion surface – consequently, in order to be conservative we illustrate the convergence below using a mass of 10^{-6} eV. Thus it should be understood that all time averaged quantities and larger axion masses have far stronger convergence than presented here.

In the left panel of Fig. 14 we show the convergence test using an $N_{\rm side} = 16$ healpix map, and for $N_{\rm photons} = 2.5 \times 10^5$, 10^6 and 4×10^6 trajectories. As an aside, we note that on a single core, generating 10^6 trajectories in our fiducial model requires approximately between 4 and 20 hours (the time is largely driven by the fractional number of photon trajectories which undergo strong reflections, something which is strongly correlated with e.g. the radial size of the conversion surface, as these trajectories prove to be the most difficult to accurately resolve with high precision) – this can be straightforwardly parallelized across an arbitrary number of cores. One can see from Fig. 14 that for maps with order $\mathcal{O}(\text{few} \times 10^6)$ photons, roughly 90% of pixels achieve convergence at the $\mathcal{O}(20\%)$ level (in order to aide the reader, we shade the 90% containment area of the histograms). If we now consider that our time domain analysis is performed using angular patches on the sky roughly half the size than what is generated from an $N_{\rm side} = 16$ pixel, we expect $\mathcal{O}(10^7)$ photons will be enough to generate sufficient convergence in these analyses. In order to verify this estimate we illustrate in the right panel of Fig. 14 the time evolution of the flux shown in the right panel of Fig. 2 using various numbers of trajectories. As can be seen, only minor variations in the time profile appear for $\gtrsim 5 \times 10^6$ trajectories, suggesting this number is indeed sufficient. All plots in this work are therefore generated using 10^7 trajectories.

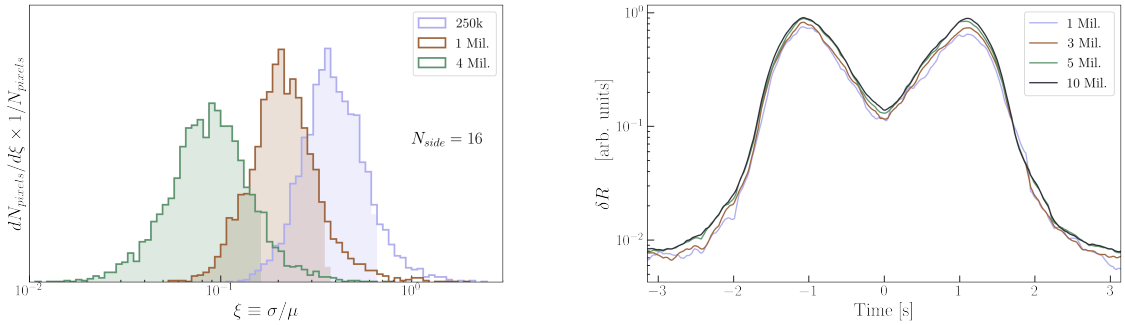

FIG. 14. Histogram of $\xi \equiv \sigma/\mu$ in each pixel of an $N_{\rm side} = 16$ healpix map, generated using 250 thousand, 1 million, or 4 million trajectories. Shading illustrates 90% containment for each histogram (left). Time slice shown in right panel of Fig. 2, varying the number of photon trajectories to illustrate the typical level of convergence (right).